chemosensors

MDPI

Article

A Highly Sensitive Coreless Fiber SPR Sensor Based on Au/TiO_2 Hyperbolic Metamaterials

Fang Wang [1], Qiwei Guo [1], Jintao Cai [1], Lening Sun [1], Lin Zhang [2] and Xuewen Shu [1,*]

[1] Wuhan National Laboratory for Optoelectronics & School of Optical and Electronic Information, Huazhong University of Science and Technology, Wuhan 430074, China; wf1742702335@163.com (F.W.); m202473524@hust.edu.cn (Q.G.); d202080928@hust.edu.cn (J.C.); m202373403@hust.edu.cn (L.S.)
[2] Aston Institute of Photonic Technologies, Aston University, Birmingham B4 7ET, UK; l.zhang@aston.ac.uk
* Correspondence: xshu@hust.edu.cn

Abstract

In this work, we propose a hyperbolic metamaterials (HMMs)-based coreless fiber surface plasmon resonance (SPR) sensor. Leveraging the absence of a core in coreless fibers, the evanescent waves at the cladding–external solution interface couple more effectively into the solution, enabling surface plasmon resonance without any additional processing. To enhance sensitivity, we adopted a multimode–coreless–multimode (MCM) structure and grew layered hyperbolic metamaterials as the SPR-excitation-sensitive layer within the coreless region. Through finite element simulations, we optimized HMM parameters and fabricated high-performance HMM-SPR sensors. Test results demonstrate that the fabricated HMM-SPR sensor achieves an optimal refractive index sensitivity of 3703.33 nm/RIU, representing a 49.68% improvement over single-layer gold film SPR sensors. It successfully detects glucose solutions at varying concentrations with a sensitivity of 2671.25 nm/RIU. The high-sensitivity, structurally simple HMM-SPR sensor we proposed demonstrates broad application prospects in biosensing, environmental monitoring, food safety, and other fields.

Keywords: surface plasmon resonance; hyperbolic metamaterials; coreless fiber; optical fiber sensors; glucose detection

1. Introduction

Surface plasmon resonance (SPR) sensors represent one of the most feasible and effective technologies for detecting minute changes in the refractive index (RI) of surrounding media, offering advantages such as label-free operation, real-time detection, and high throughput [1,2]. SPR arises from surface plasmon resonance excited by the interaction between incident light and free electrons near the interface between a dielectric and a metal film. The principle of SPR fiber optic sensors involves utilizing the evanescent field leaking from the cladding to sense the refractive indices (RIs) of the surrounding medium. When the refractive index of the medium changes, the resonance peak of the spectrum shifts. By recording wavelength shifts at different refractive indices, refractive index detection is achievable.

However, conventional SPR sensors suffer from limited detection depth at the interface and low sensitivity. Hyperbolic metamaterials (HMMs) effectively excite bulk plasmon polaritons (BPPs), exhibiting extreme sensitivity to any dielectric constant changes within the evanescent field [3], making them an excellent solution to these issues. Traditional

Check for updates

Received: 24 April 2026
Revised: 11 June 2026
Accepted: 13 June 2026
Published: 17 June 2026

Copyright: © 2026 by the authors. Licensee MDPI, Basel, Switzerland. This article is an open access article distributed under the terms and conditions of the Creative Commons Attribution (CC BY) license.

plasmonic sensors face significant challenges in detecting small molecules (molecular weight < 500 Da), exhibiting limited detection depth at the interface and issues such as low sensing sensitivity. Hyperbolic materials, characterized by unique properties, anisotropy, and distinct dielectric constant signs, have garnered increasing research attention. They represent a promising solution to these challenges and hold substantial application potential in sensor technology.

HMM-SPR sensors are primarily categorized into traditional prism sensors [4–9] and novel fiber-based sensors [10–12]. The former requires large optical components that are costly and challenging to miniaturize. In contrast, the latter offers significant advantages, including ease of integration, user-friendly operation, high flexibility, remote sensing capability, and low cost. Therefore, various fiber structures have been explored, such as D-shaped fibers [13–15], tapered fibers [16–18], and U-shaped fibers [19–21], among others, to enhance the performance of fiber optic sensors. Yang et al. fabricated a D-shaped fiber (D-POF) surface plasmon resonance (SPR) sensor [3] based on a silver and magnesium fluoride HMM, where the metal duty ratio and number of layers were 0.5 and 3, respectively. In tests with 10–50% ethanol solutions, an outstanding refractive index sensitivity of 1875 nm/RIU was achieved. Finally, they also tested solutions of varying concentrations of saccharin and BHT, achieving refractive index sensitivities of 1861.5 nm/RIU and 1854.8 nm/RIU, respectively. Gao et al. fabricated an SPR refractive index sensor [7] using a hyperbolic metamaterial composed of alternating Ag/TiN_xO_y thin films. Introducing O into TiN resulted in a positive effective dielectric constant for TiN_xO_y, creating a material with an extremely low loss coefficient suitable for the dielectric layer of the HMM. Test results demonstrate that the HMM device exhibits excellent response to refractive index changes in the near-infrared band, with a sensitivity of 2475.20 nm/RIU. The response to incident angle was also tested, yielding a sensitivity of 82.22°/RIU. Gao et al. fabricated a D-type fiber sensor combining hyperbolic metamaterials with graphene for DNA hybridization detection [22]. By integrating hyperbolic metamaterials with graphene, the sensor achieved a sensitivity of 5000 nm/RIU and a quality factor of 40 RIU^{-1}. PBASE molecules were incorporated into the graphene layer to detect probe DNA molecules at varying concentrations. Despite these advancements, existing fiber SPR sensors still face certain challenges. Conventional intact single-mode or multimode fiber SPR sensors exhibit limited evanescent field penetration depth, which significantly restricts their sensitivity. While micro-structured or side-polished fibers (such as D-type fibers) can overcome this depth limitation, they often require complex and costly fabrication processes.

To address these challenges, we propose an HMM-based coreless fiber SPR sensor in this work. Since coreless fibers lack a core, the cladding directly contacts the external solution. The evanescent waves at the cladding–solution interface couple more effectively into the solution, enabling surface plasmon resonance (SPR) without any additional treatment. To effectively couple light into and out of the sensing region and facilitate practical measurements, a multimode–coreless–multimode (MCM) fiber structure is employed. A layered HMM is immobilized within the coreless region as the SPR-exciting sensing layer. Further, we selected Au and TiO_2 as layered HMMs. Through finite element simulations of material dispersion characteristics, dielectric constants, and other parameters, we optimized the metal duty ratio ρ (metal filling fraction) and the number of layered HMM layers N_{bi} (number of bilayers) to design a high-performance HMM-SPR sensor. Ultimately, based on the sensor's performance parameters, FOM (figure of merit), we established the optimal parameters as $\rho = 0.7$, $N_{bi} = 2$. Through practical testing, the HMM-SPR sensor we designed and fabricated achieved a sensitivity of 3703.33 nm/RIU, representing a 49.68% improvement over single-layer gold film Au-SPR sensors. As a vital component of the human body, glucose rapidly replenishes blood sugar levels, alleviates hunger, and restores

blood volume. Detecting glucose concentration holds significant medical importance. We employed the fabricated HMM-SPR sensor to perform sensing tests on glucose solutions. Results demonstrated the sensor's capability to detect glucose at varying concentrations with a sensitivity of 2671.25 nm/RIU. The test results demonstrate that this work proposes a highly sensitive, structurally simple HMM-SPR sensor with broad application prospects in biosensing, environmental monitoring, food safety, and other fields.

It is worth noting that the preliminary conceptual framework of this multimode–coreless–multimode (MCM) HMM-SPR sensor was initially introduced in our previous conference proceeding [23]. Compared to that preliminary study, which primarily focused on basic structural simulations and parameter optimization, this manuscript presents a comprehensive and systematic advancement. Specifically, we delve deeply into the underlying physical mechanisms of BPPs' excitation and complex dispersion properties. Furthermore, we provide detailed experimental fabrication protocols alongside rigorous material characterizations (including SEM and EDS mapping). Most importantly, this work systematically evaluates the sensor's stability and repeatability and experimentally demonstrates its practical utility in high-sensitivity glucose concentration detection, highlighting its vast potential for real-world biosensing applications.

2. Sensor Design

To achieve higher sensing sensitivity, we adopted a multimode–coreless–multimode (MCM) fiber structure. The multimode fiber has a cladding diameter of 125 μm and a core diameter of 62.5 μm, while the coreless fiber has a diameter of 125 μm. A layered HMM hybrid metal–metal structure is fixed in the coreless region as the SPR-exciting sensitive layer, composed of Au and TiO_2 materials. Figure 1a shows a schematic of the HMM-SPR sensor. Figure 1b presents a cross-sectional schematic of the sensor at the coreless fiber location.

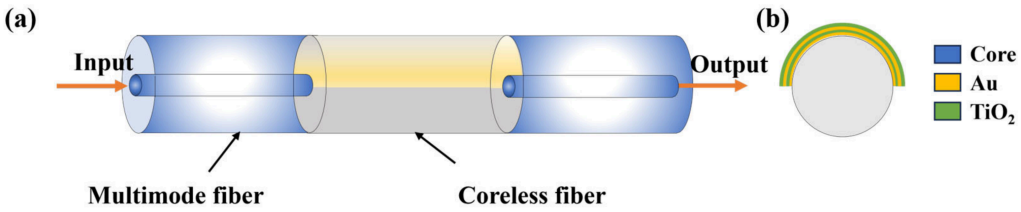


Figure 1. (**a**) Schematic diagram of the HMM-SPR sensor structure; (**b**) schematic cross-section of the HMM-SPR sensor at the coreless fiber region.

To investigate hyperbolic dispersion characteristics, we analyzed the dispersion of the Au and TiO_2 material combination. The structure of the hyperbolic metamaterial is shown in Figure 2a. The thickness of the Au and TiO_2 pair in the HMM is 30 nm, which is much smaller than the operating wavelength and satisfies the long-wave limit. This allows the parallel and perpendicular components of the HMM dielectric constant to be obtained using the Effective Medium Theory (EMT) ([1]). EMT can be described by the following formula:

$$\varepsilon_x = \rho\varepsilon_m + (1-\rho)\varepsilon_d \quad (1)$$

$$\varepsilon_z^{-1} = \rho\varepsilon_m^{-1} + (1-\rho)\varepsilon_d^{-1} \quad (2)$$

$$\rho = d_m/(d_m + d_d) \quad (3)$$

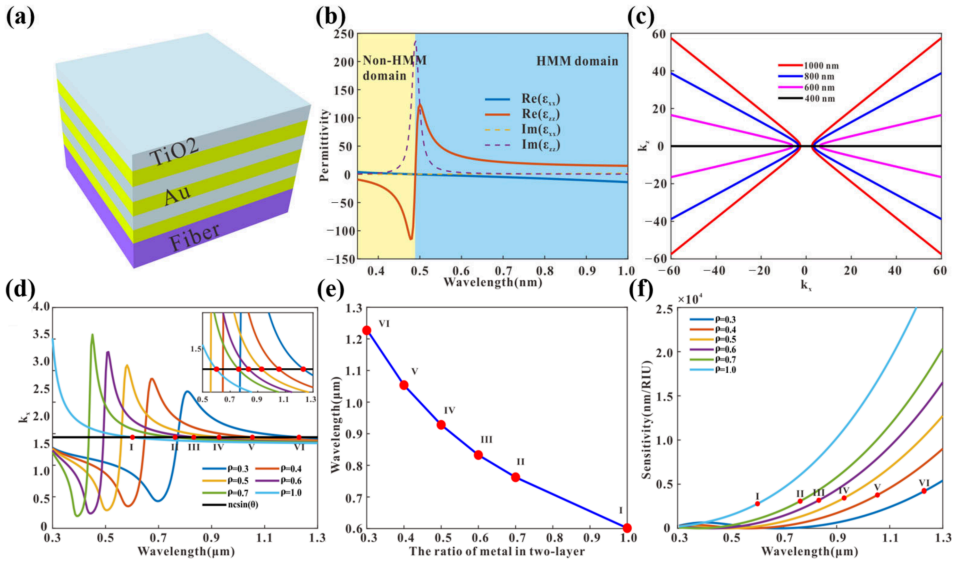


Figure 2. (**a**) Schematic of the multilayer metamaterial structure at $\rho = 0.5$ and $N_{bi} = 3$; (**b**) determination of the actual dielectric constant components of the HMM using effective medium theory; (**c**) real-part relationship curves for $\rho = 0.5$, k_z and k_x with different colors representing different wavelengths; (**d**) relationship between wavelength and effective refractive index k_x, where ρ = 1″ denotes Au and $ncsin\theta$ denotes incident light; (**e**) resonance wavelength variation curves under different metal duty cycles; (**f**) theoretical sensitivity versus wavelength curves under varying metal duty cycles, where the red dots (I–VI) indicate the specific sensitivities at their corresponding resonance wavelengths.

Here, ε_x and ε_z represent the horizontal and vertical components of the HMM dielectric constant, respectively; ε_m and ε_d denote the dielectric constants of Au and TiO_2, respectively; d_m and d_d denote their corresponding thicknesses. The metal duty ratio ρ is defined as the ratio of the Au thickness to the thickness of the HMM pair. When $\lambda \geq 490$ nm, the real part of the dielectric constant components exhibits opposite signs: $\varepsilon_{xx} = \varepsilon_{zz}, \varepsilon_{xx}\varepsilon_{zz} < 0$, indicating hyperbolic dispersion of the HMM in this region, as shown in Figure 2b. Figure 2c displays the dispersion curves of the real parts of k_x and k_z for the formula $\left(k_x^2/\varepsilon_z\right) + \left(k_z^2/\varepsilon_x\right) = k_o^2$ at $\rho = 0.5$. The dispersion curve exhibits a hyperbolic shape at $\lambda \geq 490$ nm and a linear shape at $\lambda < 490$ nm. The gold and titanium dioxide permittivities ε_m and ε_d are calculated using the Drude formula, while the titanium dioxide permittivity ε_d is obtained from the following equations:

$$\varepsilon_m = 1 - \left[\lambda^2\lambda_c/\lambda_p^2(\lambda_c + i\lambda)\right] \quad (4)$$

$$\varepsilon_d = 5.913 + 0.2441/\left(\lambda^2 - 0.0803\right)] \quad (5)$$

where λ_p and λ_c represent the plasma wavelength and collision wavelength, respectively, with values of 168.26 nm and 8934.2 nm, respectively.

Based on the SPR coupling formula for optical fibers $k_o n_c \sin\theta = k_o\sqrt{(\varepsilon_{xr} n_s^2)/(\varepsilon_{xr} + n_s^2)}$, we can derive the relationship between the resonance wavelength and the effective refractive index k_x, as shown in Figure 2d. The intersection points of the $ncsin\theta$ and ρ curves represent the resonance wavelengths, marked as red dots I, II, III, IV, V, and VI in all subfigures of Figure 2d, corresponding to wavelengths of 1229.6 nm, 1053.8 nm, 928.1 nm, 832.7 nm, 762.3 nm, and 601.5 nm, respectively. As ρ increases from 0.3 to 0.7, the resonant wavelength of the hyperbolic metamaterial sensor undergoes a blueshift, moving from 1229.6 nm to 601.5 nm, as shown in Figure 2e.

The sensitivity was calculated using the sensitivity formula $S = 2\varepsilon_x^2/\left(n_s^3 * \left|d\varepsilon_x/d\lambda\right|\right)$ for different ρ values [2]. As shown by the red dots (I to VI) in Figure 2f, which correspond

to the respective resonance wavelengths, when ρ equals 1, 0.7, 0.6, 0.5, 0.4, and 0.3, the maximum theoretical sensitivities at these resonance dips were 2785.38 nm/RIU, 3074.94 nm/RIU, 3178.03 nm/RIU, 3435.27 nm/RIU, 3773.57 nm/RIU, and 4276.80 nm/RIU, respectively. It can be observed that the resonance sensitivity exhibits a decreasing trend with increasing ρ. The results demonstrate that we can tune the resonance wavelength by controlling the metal duty ratio of the HMM, which in turn affects the sensing sensitivity.

Furthermore, we employed COMSOL Multiphysics software (version 6.3) to evaluate the geometric and performance parameters of our fundamental sensor model. Figure 3 illustrates the variation in transmission of the HMM-SPR sensor across different metal duty cycles ρ and hypermaterial layer counts N_{bi}. As shown in Figure 3a, the resonance wavelength and resonance depth of the SPR sensor shift with changes in metal duty cycle. When N_{bi} = 3, increasing the metal duty cycle causes the resonance wavelength to blueshift, the full width at half maximum (FWHM) to gradually decrease, and the resonance depth to progressively diminish. Figure 3b shows the transmittance variation of the HMM-SPR sensor for different ρ under RI = 1.34, exhibiting a similar trend to the resonance wavelength changes. Figure 3c,d display the transmittance variations of the HMM-SPR sensor with different N_{bi} values under ambient refractive indices of RI = 1.33 and RI = 1.34, respectively. For a fixed metal duty cycle of ρ = 0.6, both figures demonstrate a consistent trend: as the number of hyperbolic metamaterial layers N_{bi} increases, the resonance wavelength undergoes a notable redshift, the full width at half maximum (FWHM) gradually broadens, and the resonance depth decreases. By comparing Figure 3d with Figure 3c, it is evident that the overall resonance spectra shift toward longer wavelengths as the ambient RI increases from 1.33 to 1.34, which confirms the SPR sensing capability across different N_{bi} configurations. When N_{bi} reaches 5, the resonance depth of the SPR sensor becomes negligible. This indicates that at this point, due to excessive material thickness, the surface plasmon electric field is nearly completely attenuated, rendering high-sensitivity SPR sensing unfeasible.

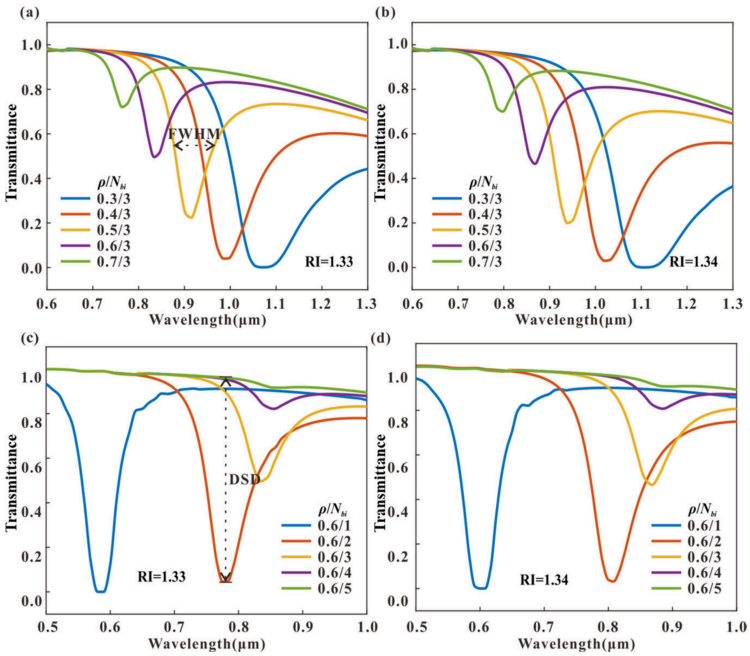


Figure 3. (**a**) Spectral curves of HMM-SPR sensors for different ρ at RI = 1.33, N_{bi} = 3; (**b**) spectral curves of HMM-SPR sensors for different ρ at RI = 1.34, N_{bi} = 3; (**c**) spectral curves of HMM-SPR sensors for different N_{bi} at RI = 1.33, ρ = 0.6; (**d**) spectral curves of HMM-SPR sensors for different N_{bi} at RI = 1.34, ρ = 0.6.

To comprehensively analyze the effects of the HMM metal duty cycle ρ and double-layer count N_{bi} on sensor performance, we calculated the trends in resonance depth (RD), full width at half-maximum (FWHM), sensitivity (SEN), and figure of merit (FOM) for sensors under different metal duty cycles and double-layer counts. Figure 4a shows FWHM variations with ρ and N_{bi}. When N_{bi} remains constant, FWHM gradually decreases with increasing ρ. When ρ remains constant, FWHM gradually increases with increasing N_{bi}. Figure 4b shows RD variations with ρ and N_{bi}. When N_{bi} remains constant, RD gradually decreases with increasing ρ. When ρ remains constant, RD gradually decreases with increasing N_{bi}. The maximum RD value equals 1, indicating peak coupling efficiency. Figure 4c shows sensitivity variation with ρ and N_{bi}. When N_{bi} remains constant, sensitivity gradually increases with ρ before plateauing at a maximum of 4548.49 nm/RIU. When ρ remains constant, sensitivity gradually increases with N_{bi}. Figure 4d shows the FOM variation with ρ and N_{bi}. When N_{bi} remains constant, the FOM gradually increases with increasing ρ. When ρ remains constant, the FOM first increases and then decreases with increasing N_{bi}. Here, FOM is adopted as the comprehensive evaluation criterion. When ρ and N_{bi} are 0.7 and 2, respectively, the FOM reaches a maximum of 42.9, selected as our optimal design parameters.

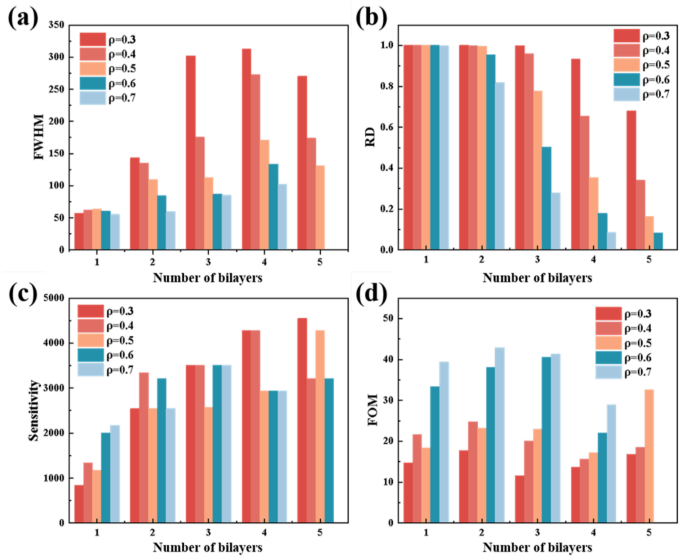


Figure 4. (**a**) Variation of FWHM with different ρ and N_{bi}; (**b**) variation of RD with different ρ and N_{bi}; (**c**) variation of SEN with different ρ and N_{bi}; (**d**) variation of FOM with different ρ and N_{bi}.

To unveil the underlying physical mechanism, the exceptional performance under the optimal parameters (ρ = 0.7 and N_{bi} = 2) is closely correlated with the unique dispersion properties of the HMM. Compared with a conventional single-layer gold film where surface plasmon polaritons (SPPs) are strictly bounded at the single metal/dielectric interface with a rapidly decaying evanescent field, the alternating Au/TiO_2 subwavelength multilayers support BPPs that propagate within the metamaterial volume. When the metal duty cycle ρ is optimized at 0.7, the effective permittivity components parallel and perpendicular to the fiber surface exhibit a strong hyperbolic anisotropy. This particular configuration maximizes the electromagnetic field confinement and significantly extends the penetration depth of the evanescent field into the surrounding analyte. Consequently, the overlap integral between the optical mode and the external solution is drastically enhanced, boosting the refractive index sensitivity.

Furthermore, the bilayer count N_{bi} = 2 acts as the crucial balancing point for the FOM. When N_{bi} = 1, the multi-interface coupling effect is insufficient to form a robust hyperbolic medium. Conversely, when N_{bi} exceeds 2, although the stronger BPP excitation might

slightly shift the resonance position, the excessive total thickness induces severe intrinsic Ohmic losses from the additional gold layers. This over-damping effect results in drastic spectral broadening (larger FWHM) and a diminished resonance depth, which ultimately degrades the FOM. Therefore, the architecture with $\rho = 0.7$ and $N_{bi} = 2$ represents the exact physical spot where BPP excitation efficiency and evanescent-field penetration depth are maximized while keeping the parasitic Ohmic attenuation well-controlled.

3. Fabrication and Characterization

We first fabricate an Au-film SPR sensor as a reference device. Its fabrication mainly comprises two steps: preparing the MCM fiber structure and depositing an Au layer on the sensing region, as illustrated in Figure 5a. The multimode fiber has a core diameter of 62.5 μm and a cladding diameter of 125 μm. The coreless fiber lacks a core and has a cladding diameter of 125 μm. First, use wire strippers to remove the cladding from a specific length of the multimode fiber. Then, trim the excess fiber with a fiber cutter to retain the appropriate length and clean the end with alcohol. Subsequently, use stripping pliers to remove the cladding from a specific length of coreless fiber and, similarly, clean with alcohol. Then, fuse the coreless fiber with two multimode fibers by using the fiber fusion splicer to obtain the desired MCM structure. The sensing region comprises two 0.5 cm cladding-stripped multimode fiber segments and a 1 cm coreless fiber section between them. Finally, a gold film was deposited on one side of the sensing region using an electron beam evaporation coating system (Ohmiker-50B, Cello Technology Co., Ltd., Hsinchu, Taiwan, China). The thickness of the gold layer was controlled by adjusting the discharge time and current.

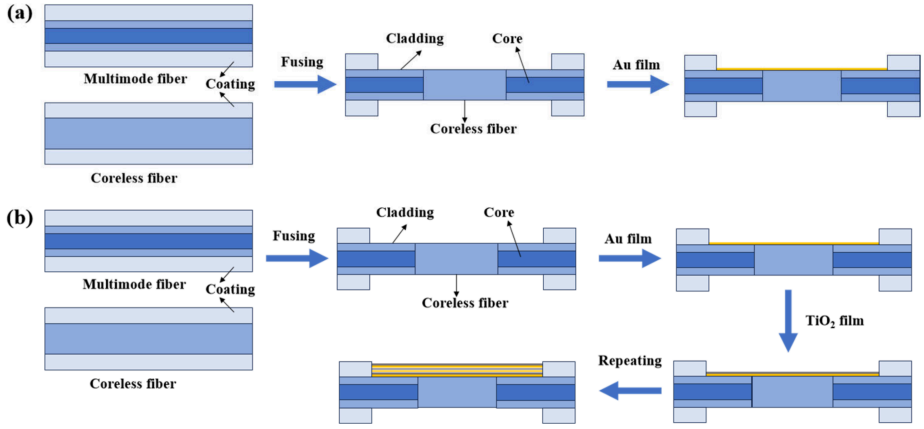


Figure 5. (**a**) Schematic of Au-SPR sensor fabrication; (**b**) schematic of HMM-SPR sensor fabrication. The yellow and grey layers represent the deposited Au film and TiO_2 film.

The fabrication process of the HMM-SPR sensor is shown in Figure 5b. The preparation procedure for the MCM fiber structure is identical to that of the gold-film SPR sensor. After obtaining the suitable MCM structure, alternating deposition of Au and TiO_2 layers is performed on the sensing region. During deposition, the vacuum chamber pressure was maintained at 8×10^{-6} Torr. Gold was thermally evaporated from a gold target at a rate of 2 Å/s (1 Å = 0.1 nm), depositing a 21 nm thick gold film onto the sensing region of the MCM. Subsequently, the 9 nm thick TiO_2 layer was deposited onto the gold film using magnetron sputtering. At this stage, the vacuum chamber pressure was maintained at 9×10^{-4} Torr, with an evaporation rate of 9 Å/min. This process was repeated to obtain the desired HMM-SPR sensor.

Furthermore, we performed material characterization on the fabricated sensors. To clearly visualize the alternating multilayer architecture of the fabricated HMM, the

3*Au/TiO_2 configuration was deliberately selected as a representative sample for SEM and EDS characterizations. Since the individual Au and TiO_2 layers are extremely thin (21 nm and 9 nm, respectively), a sample with a higher number of bilayers (N_{bi} = 3) provides significantly better visual contrast and morphological clarity to verify the successful alternating deposition process. Cross-sectional images of the Au-SPR and HMM-SPR sensors were captured using scanning electron microscopy (SEM). Figure 6b,c show SEM images of the gold film sensor, revealing a uniformly distributed gold film approximately 60 nm thick grown on the fiber surface. Figure 6d,e present SEM images of the HMM-SPR sensor. These reveal a distinct multilayer structure within the HMM comprising an Au film (21 nm) and a TiO_2 film (9 nm). The fabricated HMM structure exhibits excellent uniformity, with the prepared thickness falling within the simulated design range. The EDS spectrum (EDS, X-Max, Oxford Instruments, Abingdon, UK) and EDS element distribution maps are shown in Figures 6f and 6h,i, respectively. The EDS spectrum indicates the presence of Au, Ti, and O elements in the metamaterial, with uniform distribution.

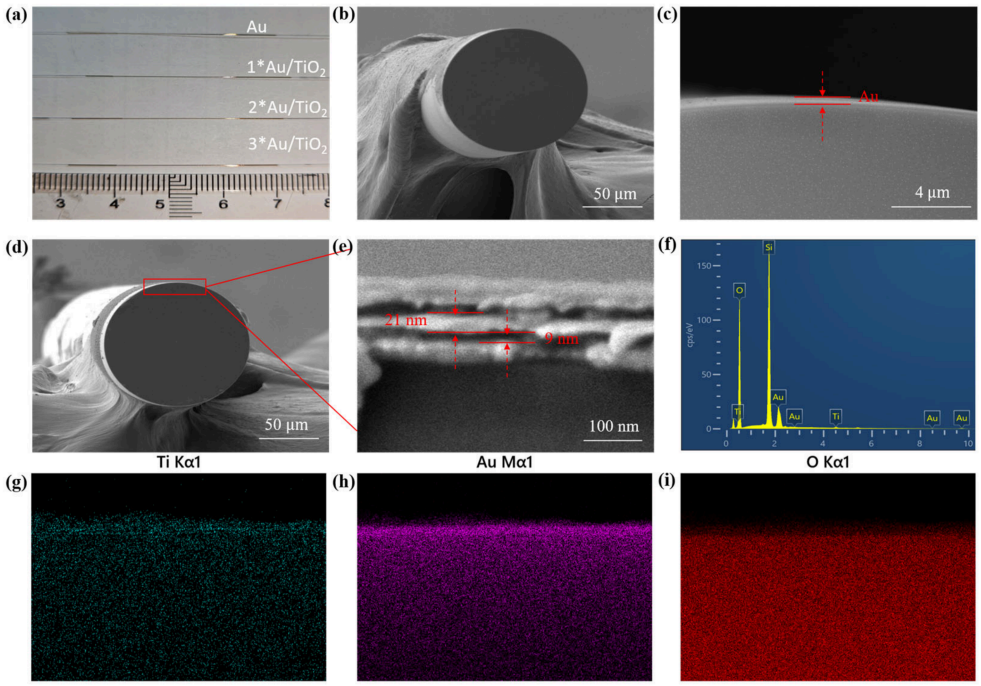


Figure 6. (**a**) Photographs of the Au-SPR sensor and the 3*Au/TiO_2/HMM-SPR sensor; (**b**) SEM image of the 60 nm gold film sensor; (**c**) cross-sectional view of the 60 nm gold film sensor; (**d**) SEM image of the 3*Au/TiO_2/HMM-SPR sensor; (**e**) cross-section of the 3*Au/TiO_2/HMM-SPR sensor; (**f**) EDS elemental map of the 3*Au/TiO_2/HMM-SPR sensor; (**g**–**i**) EDS elemental distribution maps of Ti, Au, and O elements in the 3*Au/TiO_2/HMM-SPR sensor; numbers 1–3 denote the logarithmic values of Au/TiO_2 material deposited on the sensing region of the Au/TiO_2/HMM-SPR sensor.

4. Experimental Results

The SPR-sensor-testing system is shown in Figure 7. We fixed the optical fiber in the test chamber and introduced glycerol solutions of different refractive indices into the chamber via a pipette for refractive index sensing tests. For accurate measurements, the sensor was cleaned with deionized water and alcohol before each measurement. The test light source was a halogen lamp (HL-2000, Idea Optics Instruments, Shanghai, China) with a wavelength range of 360–2000 nm. Spectral changes in the SPR resonance peak were recorded by a spectrometer (PG 2000, Idea Optics Instruments, Shanghai, China). The other end of the spectrometer was connected to a computer, enabling real-time measurement and recording of the transmission spectrum via specialized spectral analysis software.

The refractive index solutions used in testing were prepared by mixing glycerol with deionized water at varying ratios, yielding a refractive index range of 1.3330–1.3901. The corresponding test results are shown below.

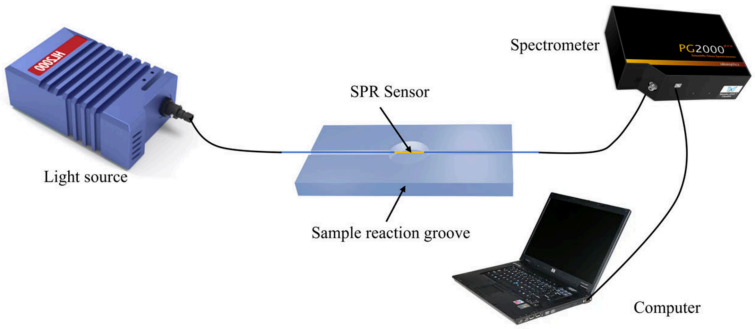


Figure 7. Schematic diagram of the experimental setup.

It is worth noting that temperature cross-sensitivity is a critical consideration in SPR sensing systems, as both the refractive indices of the liquid analytes (e.g., glycerol and glucose solutions) and the dielectric properties of the metamaterial layers are C. To strictly eliminate temperature-induced spectral fluctuations, all sensing experiments in this study were conducted in a meticulously controlled constant-temperature environment maintained at 25 ± 0.5 °C. Both the liquid samples and the testing platform were allowed to reach thermal equilibrium prior to each measurement. This rigorous thermal management ensures that the observed resonance wavelength shifts are exclusively attributed to the variations in the bulk refractive index of the solutions, thereby ensuring the reliability of the sensing data.

Figure 8a–c show normalized spectra of a HMM-SPR sensor with different double-layer numbers measuring solutions of varying refractive indices. The insets depict schematic models of different structures. As the number of HMM layers increases, the minimum of the curve undergoes a redshift, exhibiting a trend similar to the previously simulated spectral curve. Figure 8d presents the normalized spectra of an Au-SPR sensor measuring solutions with varying refractive indices. The figure demonstrates that the resonance wavelength shifts toward longer wavelengths as the refractive index increases. Figure 8e illustrates the resonance wavelength curves of both the Au-SPR sensor and the HMM-SPR sensor as a function of refractive index. Figure 8f summarizes and compares the resonance wavelength shifts and refractive index sensitivities of the Au-SPR sensor and the Au/TiO_2/HMM-SPR sensor. Compared to the Au-SPR sensor, the resonance wavelength of the Au/TiO_2/HMM- SPR sensor increased from 598.84 nm to 737.25 nm, while the refractive index sensitivity rose from 2474.21 nm/RIU to 3733.11 nm/RIU. The Au-SPR exhibits the lowest sensitivity, corresponding to 2474.21 nm/RIU. The highest sensitivity of C corresponds to the 3*Au/TiO_2/HMM-SPR configuration. However, as shown in Figure 8c, when the HMM thickness exceeds the propagation distance of the evanescent field, the resonance wavelength becomes disordered, and spectral broadening significantly reduces the sensor's resolution. Although the 3*Au/TiO_2 configuration yields the highest absolute sensitivity (3733.11 nm/RIU), sensitivity alone is insufficient to holistically evaluate the practical performance of an SPR sensor. A comprehensive evaluation must deeply consider the FOM, which is defined as the ratio of sensitivity to the FWHM. As the number of bilayers (N_{bi}) increases to 3, the cumulative Ohmic loss from the multiple metal layers intensifies, leading to severe spectral broadening (a significantly larger FWHM). This broadening diminishes the FOM and drastically deteriorates the sensor's actual resolution, making it difficult to precisely track the resonance dip. Therefore, by balancing both the sensitivity and the

FWHM, the 2*Au/TiO_2 structure exhibits the highest FOM, representing the optimal structural configuration for practical sensing applications. Comprehensive analysis indicates that the optimal structure for the sensor is 2*Au/TiO_2/HMM-SPR, achieving a sensitivity of 3703.33 nm/RIU—representing a 49.68% improvement in refractive index sensitivity compared to Au-SPR sensors. Experimental results align with the optimal parameters derived from simulation design, further validating the scientific rigor and feasibility of the sensor design methodology.

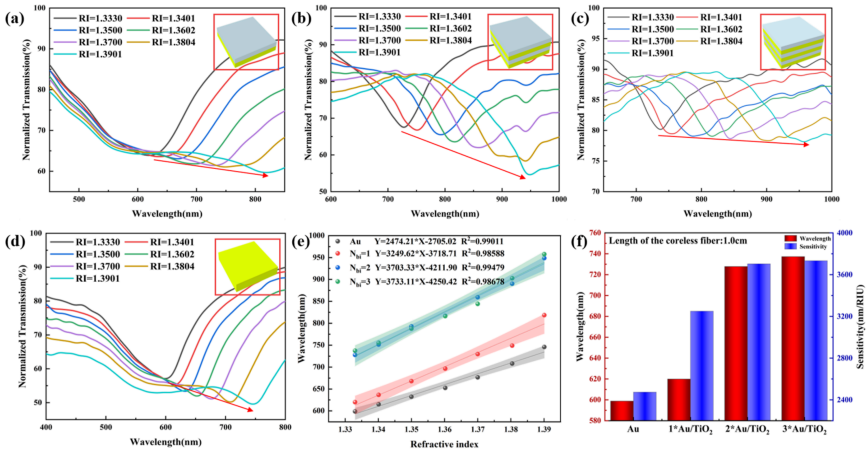


Figure 8. (**a**) Normalized spectrum of the 1*Au/TiO_2/HMM-SPR sensor; (**b**) normalized spectrum of the 2*Au/TiO_2/HMM-SPR sensor; (**c**) normalized spectrum of the 3*Au/TiO_2/HMM-SPR sensor; (**d**) normalized spectrum of the Au-SPR sensor; (**e**) resonance wavelength versus refractive index curves for the Au-SPR sensor and HMM-SPR sensors with varying layer numbers; (**f**) resonance wavelength and refractive index sensitivity of the Au-SPR sensor and HMM-SPR sensors with different layer numbers. The red arrows indicate the direction of the resonance wavelength redshift as the refractive index increases.

Sensor stability and repeatability are critical performance metrics. We conducted sensing experiments at 1 h intervals using a solution with a constant refractive index (RI = 1.3401). The sensor was placed on the test platform, and solutions with identical refractive indices were dispensed onto the platform using a pipette. The sensing area was rinsed with deionized water before each new solution test. A total of five experimental sets were conducted, with a maximum spectral shift of 0.9 nm and a variance of 0.1134 across the five sets, indicating excellent stability of the fabricated sensor. The test results are shown in Figure 9a,b. To demonstrate the sensor's repeatability, we performed repeated measurements on the same sensor using the identical experimental setup at 14-day intervals. The obtained data underwent linear fitting, as shown in Figure 9c. The sensitivities measured at different time points were 3703.33 nm/RIU and 3723.92 nm/RIU, respectively. This result confirms the sensor's excellent repeatability and stability.

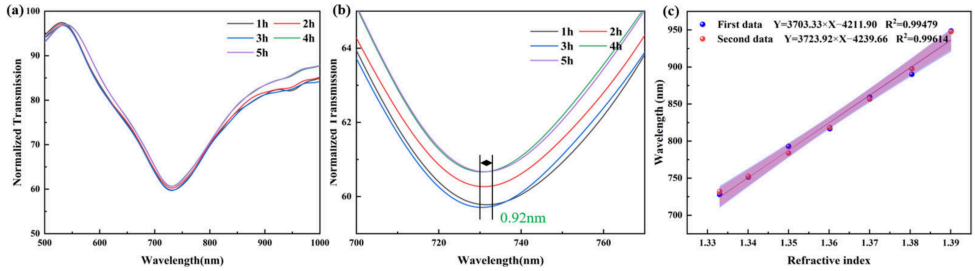


Figure 9. (**a**) Spectral curves of the sensor recorded every hour in a solution with an identical refractive index; (**b**) localized enlargement of the spectral curve in (**a**); (**c**) repeatability test results of the sensor.

Glucose is a vital component of the human body, rapidly replenishing blood sugar, alleviating hunger, and restoring blood volume. Monitoring glucose concentration holds significant medical importance. To further evaluate the sensor's performance in practical biological liquid environments, glucose solutions were selected as a model analyte. We employed the fabricated HMM-SPR sensor to perform sensing tests on glucose solutions at concentrations of 0%, 1%, 5%, 10%, and 15%. The refractive indices of glucose solutions at concentrations of 0%, 1%, 5%, 10%, and 15% were measured to be 1.3330, 1.3345, 1.3395, 1.3460, and 1.3543, respectively. Figure 10 displays the normalized spectral curve changes of the HMM-SPR sensor across different refractive indices corresponding to various glucose concentrations. As glucose concentration increased from 0% to 15%, the spectrum exhibited a redshift, with the resonance wavelength extending from 734.55 nm to 790.72 nm. Figure 10b plots the resonance wavelength of the sensor as a function of the refractive index corresponding to the glucose concentration. The sensor exhibits a sensitivity of 2671.25 nm/RIU, demonstrating excellent linear response with a coefficient of determination R^2 = 0.99693.

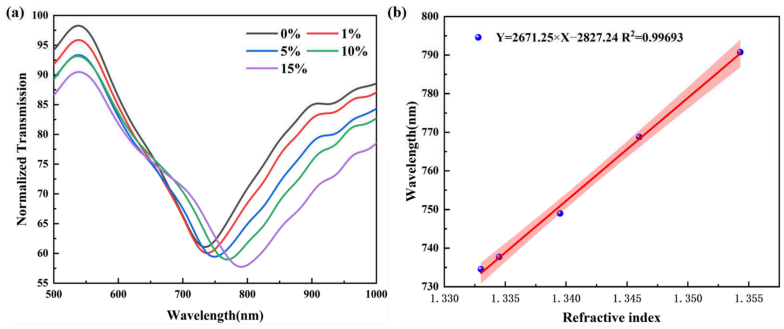


Figure 10. (**a**) Spectral curves of the HMM-SPR sensor at glucose concentrations ranging from 0% to 15%; (**b**) functional curve of the HMM-SPR sensor's resonance wavelength as a function of the refractive index corresponding to the glucose concentration.

It should be noted that the current bare HMM-SPR architecture lacks specific biochemical functionalization and fundamentally operates as a highly sensitive bulk refractive index sensor. Therefore, while it exhibits excellent responsiveness to the refractive index variations induced by glucose, the response is inherently non-specific. Nevertheless, these experimental results successfully demonstrate the device's outstanding capability for bioliquid refractive index sensing, laying a solid foundation for the future development of highly specific biosensors through selective surface modification.

Table 1 compares the performance of the HMM sensor fabricated in this study with other plasmonic sensors. Compared with other works, the HMM sensor designed and fabricated in this study exhibits superior sensing sensitivity, achieving a bulk sensitivity as high as 3703.33 nm/RIU.

Table 1. Comparison of the HMM sensor prepared in this paper with other plasmonic sensors.

Structure Type	Sensitive Material	Fabrication Method	Refractive Index Range	Operating Bandwidth	Sensitivity (nm/RIU)
MCM [24]	Au	Magnetron sputtering	1.330–1.3883	Visible light	2249.33
D-type fiber [25]	Ag/MgF_2	Magnetron sputtering	1.333–1.360	Visible light	1603
Plastic fiber [1]	Au/AuNPs	Sputtering ion machine	1.332–1.361	Visible light	1956/2787
D-type fiber [3]	HMM	Thermal deposition	1.34–1.356	Visible light	1875
Tapered fiber [16]	Au	Magnetron sputtering	1.3327–1.371	Visible light	1841.86
D-type fiber [26]	Au/AuNPs	Vacuum ion beam sputtering	1.3332–1.371	Visible light	3074
MCM (This paper)	HMM	Sputtering + electron beam evaporation	1.333–1.3901	Visible light	3703.33

5. Conclusions

In summary, we propose a coreless fiber SPR sensor based on HMMs. By utilizing coreless fiber, more surface plasmon polaritons at the interface can be coupled into the deposited HMM structure. The sensing performance was systematically evaluated across a solution refractive index range of 1.3330 to 1.3901. The optimal HMM sensor structure achieved a sensitivity of 3703.33 nm/RIU, representing 49.68% improvement over single-layer gold film sensors. Finally, the fabricated HMM-SPR ($\rho = 0.7$, $N_{bi} = 2$) sensor was employed to detect glucose solution concentrations. Experimental results demonstrated the sensor's capability to detect glucose at varying concentrations with a sensitivity of 2671.25 nm/RIU. By overcoming the limited penetration depth of conventional SPR sensors, this highly sensitive and structurally simple HMM-based device paves a new way for real-time biochemical analysis, showing great promise in clinical health monitoring and biochemical sensing.

Author Contributions: Conceptualization, F.W. and X.S.; methodology, F.W., L.Z. and X.S.; investigation, F.W. and J.C.; writing—original draft preparation, F.W.; writing—review and editing, Q.G., L.S., L.Z. and X.S.; supervision, X.S.; funding acquisition, X.S. All authors have read and agreed to the published version of the manuscript.

Funding: This work was supported by the National Key R&D Program of China (2023YFE0105800) and the National Natural Science Foundation of China (62275093).

Institutional Review Board Statement: Not applicable.

Informed Consent Statement: Not applicable.

Data Availability Statement: The original contributions presented in this study are included in the article. Further inquiries can be directed to the corresponding author.

Conflicts of Interest: The authors declare no conflicts of interest.

References

1. Zheng, W.-L.; Zhang, Y.-N.; Li, L.-K.; Li, X.-G.; Zhao, Y. A plug-and-play optical fiber SPR sensor for simultaneous measurement of glucose and cholesterol concentrations. *Biosens. Bioelectron.* **2022**, *198*, 113798.
2. Dubey, S.K.; Kumar, A.; Kumar, A.; Pathak, A.; Srivastava, S.K. A study of highly sensitive D-shaped optical fiber surface plasmon resonance based refractive index sensor using grating structures of Ag-TiO_2 and Ag-SnO_2. *Optik* **2022**, *252*, 168527.
3. Yang, W.; Gao, J.; Li, Z.; Li, C.; Cheng, Y.; Huo, Y.; Jiang, S.; Jiang, M. High performance D-type plastic fiber SPR sensor based on a hyperbolic metamaterial composed of Ag/MgF_2. *J. Mater. Chem. C* **2021**, *9*, 13647–13658. [CrossRef]
4. Kabashin, A.V.; Evans, P.; Pastkovsky, S.; Hendren, W.; Wurtz, G.A.; Atkinson, R.; Pollard, R.; Podolskiy, V.A.; Zayats, A.V. Plasmonic nanorod metamaterials for biosensing. *Nat. Mater.* **2009**, *8*, 867–871. [CrossRef] [PubMed]
5. Sreekanth, K.V.; Alapan, Y.; Elkabbash, M.; Ilker, E.; Hinczewski, M.; Gurkan, U.A.; De Luca, A.; Strangi, G. Extreme sensitivity biosensing platform based on hyperbolic metamaterials. *Nat. Mater.* **2016**, *15*, 621–627. [CrossRef] [PubMed]
6. Chen, Y.; Hu, S.; Wang, H.; Zhi, Y.; Luo, Y.; Xiong, X.; Dong, J.; Jiang, Z.; Zhu, W.; Qiu, W.; et al. MoS_2 Nanosheets Modified Surface Plasmon Resonance Sensors for Sensitivity Enhancement. *Adv. Opt. Mater.* **2019**, *7*, 1900479. [CrossRef]
7. Gao, H.-Z.; Xu, W.-R.; Li, M.-C.; Ilyas, N.; Wang, J.-M.; Li, W.; Jiang, X.-D. Hyperbolic metamaterials based on multilayer Ag/TiN_xO_y structure for SPR refractive index sensors. *Opt. Laser Technol.* **2022**, *151*, 108034. [CrossRef]
8. Yan, R.; Wang, T.; Yue, X.; Wang, H.; Zhang, Y.; Xu, P.; Wang, L.; Wang, Y.; Zhang, J. Highly sensitive plasmonic nanorod hyperbolic metamaterial biosensor. *Photonics Res.* **2022**, *10*, 84–95.
9. Zhao, B.; Sang, L.; Zhang, Z.; Chen, X.; Li, M.; Li, Y.; Xue, Y.; Yan, T.; Wang, B.; Jian, A. Genetic algorithm-optimized hyperbolic metamaterial SPR sensors for ultrasensitive biosensing. *Appl. Anal. Chem.* **2026**, *98*, 11769–11778. [CrossRef] [PubMed]
10. Zhao, Y.; Deng, Z.-Q.; Wang, Q. Fiber optic SPR sensor for liquid concentration measurement. *Sens. Actuators B Chem.* **2014**, *192*, 229–233. [CrossRef]
11. Shrivastav, A.M.; Mishra, S.K.; Gupta, B.D. Fiber optic SPR sensor for the detection of melamine using molecular imprinting. *Sens. Actuators B Chem.* **2015**, *212*, 404–410. [CrossRef]
12. Chen, Y.; Hu, S.; Shen, C.; Zhang, L.; Yi, C.; Chen, Y.; Liu, G.-S.; Chen, L.; Chen, Z.; Luo, Y. Hyperbolic-Metamaterial-Based Optical Fiber SPR Sensor Enhanced by a Smart Hydrogel for Perspiration pH Measurements. *Nano Lett.* **2025**, *25*, 129–137. [PubMed]

13. Dong, J.; Zhang, Y.; Wang, Y.; Yang, F.; Hu, S.; Chen, Y.; Zhu, W.; Qiu, W.; Guan, H.; Lu, H.; et al. Side-polished fewmode fiber based surface plasmon resonance biosensor. *Opt. Express* **2019**, *27*, 11348–11360. [CrossRef] [PubMed]
14. Gong, W.; Jiang, S.; Li, Z.; Li, C.; Xu, J.; Pan, J.; Huo, Y.; Man, B.; Liu, A.; Zhang, C. Experimental and theoretical investigation for surface plasmon resonance biosensor based on graphene/Au film/D-POF. *Opt. Express* **2019**, *27*, 3483–3495. [CrossRef] [PubMed]
15. Lu, X.; Yu, X.; Zhou, J.; Chang, M.; Lu, D. An Ultra-Wide Range D-Shaped Fiber SPR Sensor with a Nanostructure of Gold–MoS_2 and Sodium for the Simultaneous Measurement of Refractive Index and Temperature. *Sensors* **2025**, *25*, 377. [PubMed]
16. Wei, X.; Peng, Y.; Chen, X.; Zhang, S.; Zhao, Y. Optimization of tapered optical fiber sensor based on SPR for high sensitivity salinity measurement. *Opt. Fiber Technol.* **2023**, *78*, 103309. [CrossRef]
17. Liu, Z.; Ji, X.; Qin, Y.; Zhang, Y.; Mou, J.; Deng, Y.; Liu, W.; Zhang, Y.; Yuan, L. Refractive index SPR sensor with high sensitivity and wide detection range using tapered silica fiber and photopolymer coating. *Opt. Express* **2023**, *31*, 31768–31779. [CrossRef] [PubMed]
18. Shen, C.; Huang, J.; Hu, S.; Chen, Y.; Zhang, L.; Yi, C.; Hu, X.; Chen, Y.; Chen, L.; Liu, G.-S.; et al. Direct electronical readout of surface plasmon resonance biosensor enabled by on-fiber Graphene/PMMA photodetector. *Biosens. Bioelectron.* **2025**, *271*, 116992. [CrossRef] [PubMed]
19. Yang, W.; Yu, J.; Xi, X.; Sun, Y.; Shen, Y.; Yue, W.; Zhang, C.; Jiang, S. Preparation of Graphene/ITO Nanorod Metamaterial/U-Bent-Annealing Fiber Sensor and DNA Biomolecule Detection. *Nanomaterials* **2019**, *9*, 1154. [CrossRef] [PubMed]
20. Zhang, C.; Li, Z.; Jiang, S.Z.; Li, C.H.; Xu, S.C.; Yu, J.; Li, Z.; Wang, M.H.; Liu, A.H.; Man, B.Y. U-bent fiber optic SPR sensor based on graphene/AgNPs. *Sens. Actuators B Chem.* **2017**, *251*, 127–133. [CrossRef]
21. Yan, X.; Wang, L.; Fu, R.; Zhou, X. A U-shaped optical fiber MIP-SPR sensor for specific and rapid glucose measurement. *IEEE Sens. J.* **2026**, *26*, 12040–12048. [CrossRef]
22. Gao, J.; Jiang, S.; Yang, W.; Liu, R.; Feng, J.; Zha, Z.; Zhang, C.; Jiang, M.; Fan, X. Design of a D-shaped single-mode fiber SPR sensor with a composite nanostructure of HMM/monolayer graphene for DNA hybridization detection. *Opt. Laser Technol.* **2023**, *158*, 108854.
23. Wang, F.; Sun, L.; Cai, J.; Zhang, L.; Shu, X. SPR sensor based on hyperbolic metamaterial and coreless fiber. In Proceedings of the Conference on Lasers and Electro-Optics (CLEO) 2025, Long Beach, CA, USA, 4–9 May 2025; p. SS170-7.
24. Lang, T.; Cao, B.; Shen, C.; Shi, G. Multimode-coreless-multimode fiber biosensor based on surface plasmon resonance. *J. Phys. D Appl. Phys.* **2019**, *52*, 195204.
25. Kim, Y.-C.; Masson, J.-F.; Booksh, K.S. Single-crystal sapphire-fiber optic sensors based on surface plasmon resonance spectroscopy for in situ monitoring. *Talanta* **2005**, *67*, 908–917. [CrossRef] [PubMed]
26. Niu, L.-Y.; Wang, Q.; Jing, J.-Y.; Zhao, W.-M. Sensitivity enhanced D-type largecore fiber SPR sensor based on Gold nanoparticle/Au film co-modification. *Opt. Commun.* **2019**, *450*, 287–295. [CrossRef]

Disclaimer/Publisher's Note: The statements, opinions and data contained in all publications are solely those of the individual author(s) and contributor(s) and not of MDPI and/or the editor(s). MDPI and/or the editor(s) disclaim responsibility for any injury to people or property resulting from any ideas, methods, instructions or products referred to in the content.